Journal of Power Sources 182 (2008) 334–339

Contents lists available at ScienceDirect

Journal of Power Sources

journal homepage: www.elsevier.com/locate/jpowsour

Fast and reversible lithium-induced electrochemical alloying in tin-based composite oxide hierarchical microspheres assembled by nanoplate building blocks

Qiang Wang, Zhenhai Wen, Jinghong Li*

Department of Chemistry, Key Lab of Bioorganic Phosphorus Chemistry & Chemical Biology, Tsinghua University, Beijing 100084, China

ARTICLE INFO

Article history:
Received 14 November 2007
Received in revised form 24 March 2008
Accepted 26 March 2008
Available online 10 April 2008

Keywords:
Electrochemical alloying
Hierarchical microsphere
Tin-based composite oxide

ABSTRACT

To benefit from the large capacity gain advantages offered by lithium-induced electrochemical alloying and to overcome poor kinetics, a novel concept to tackle such issues by using porous hierarchical microspheres with an interconnected network of nanoplate building blocks, has been introduced and demonstrated with $Sn_{1.0}P_{1.17}O_{4.72}$ glass as an example. Such desired three-dimensional microarchitectures with exciting nanosize effects can be exploited to fabricate next generation of lithium-ion batteries where outstanding rate capability and sustained reversible capacity are achieved.

1. Introduction

For lithium-ion batteries, metals and semiconductors (for example tin- and silicon-based materials) that react with lithium to form alloys are among the most appealing and competitive candidates for new types of electrode materials, in which lithium-induced alloying processes are partially reversible and of low potential relative to lithium, involve a large number of atoms per formula unit, and in particular provide a specific capacity much larger than that offered by conventional intercalation reactions [1]. Unfortunately, the enormous volume changes generated during the alloying/de-alloying processes cause critical mechanical damage to the electrode, resulting in cracking and crumbling of the electrode and a remarked loss of capacity in the course of a few cycles [2–11]. Recent implementations suggest that the pulverization problems associated with the large volume difference between the lithiated and de-lithiated host can be lessened by using smaller particle morphology to reduce the absolute local volume changes of each reactive grain [12–14] and by introducing a suitable matrix to confine the volume change and dissipate local mechanical stresses [15–19].

However, such excitement needs to be tempered because ensuring rapid and reversible electrochemical alloying is an unavoidable issue. The future of such electrochemical alloying in real-life applications lies in mastering their kinetics, which is especially acute when alloying rather than intercalation electrode is used [20,21]. Though alloying performance can also benefit from nanostructuring owing to size confinement that alters particle deformation and reduces fracturing, perhaps the greatest disadvantage of primary nanoparticles is the possibility of an increase in undesirable side reactions with the electrolyte due to high surface area, leading to self-discharge, poor cycling life and safety concerns (the most critical issues for lithium-ion batteries) [1]. Additionally, in most commercial lithium-ion batteries, the separator used has approximately 1 μm diameter pores, thus nanoscale particles, if released from the electrode surface, may actually cross the barrier and agglomerate on the other electrode, degrading electrode performance and causing electrode failure [22]. Such problems might be addressed with internally nanostructured materials (defined as secondary nanomaterials), where the particles are significantly larger than the primary nanoparticles. Recently, hierarchically self-assembled microarchitecture with designed chemical components and highly specific morphologies is of particular interest to scientists not only because of its importance in understanding the concept of self-assembly with primary building blocks but also for its great potential for technological application [23–29]. As well as reducing side reactions with the electrolyte and ensuring the electrodes electronically separated, such open, porous and interconnective morphology design possesses several features of interest in the design of novel electrode materials such as continuous percolation paths and efficient intergrain electronic contacts, while maximizing the rate capability benefits of shorter diffusion

* Corresponding author. Tel.: +86 10 6279 5290; fax: +86 10 6277 1149.
E-mail address: jhli@mail.tsinghua.edu.cn (J. Li).

0378-7753/$ – see front matter © 2008 Elsevier B.V. All rights reserved.
doi:10.1016/j.jpowsour.2008.03.085

pathways at the nanoscale. Accordingly, achieving the high power and retaining a high capacity for lithium-ion batteries become possible.

In this investigation, we stuck to tin-based composite oxide (TCO) glasses [15], which have a basic formula represented by SnM_xO_y, where M is a group of glass-forming elements (such as B and P), and chose amorphous SnP_xO_y as a prototype alloying electrode material. Herein we successfully designed a facile and mild wet chemical route to organize as-formed nanoplate building components into porous hierarchical microspheres with the composition $Sn_{1.0}P_{1.17}O_{4.72}$.

2. Experimental

2.1. Synthesis

In a typical procedure, $SnCl_4$ serves as a tin source and NaH_2PO_4 serves as a phosphor source. Our TCO hierarchical microspheres were synthesized by mixing 3.1 g of $SnCl_4$ and 11.4 g of Na_2HPO_4, which was followed by dissolving 40 mL deionized water. The reaction was carried out in a beaker equipped with a Teflon-coated magnetic stirring bar at room temperature. Subsequently, 10.6 g of HF 10 wt% was added to the resultant solution with vigorous stirring. A transparent solution has been shown to readily form when HF was added to the above solution. When a clear solution was obtained, 2.9 g of sodium dodecyl sulfate (SDS) was dissolved in 20 mL of deionized water, and the resulting solution was added to a mixture solution of $SnCl_4$ and Na_2HPO_4. The mixture was stirred for 1 h and then placed into a 70 mL Teflon-lined autoclave. The autoclave was sealed, maintained at 150 °C for 12 h. After cooling to room temperature, the precipitate was recovered by centrifugation, followed by repeated washing with distilled water, and then calcined at 300 °C for 3 h.

2.2. Characterization

Powder X-ray diffraction (XRD) was performed on a Bruker D8-Advance diffractometer with monochromatized Cu Kα radiation (λ = 1.5418 Å). The 2θ range used in the measurements was from 10° to 70°. Field-emission scanning electron microscope (FESEM) images were taken with a JSM-7401F instrument using an accelerating voltage of 200 kV. X-ray photoelectron spectroscopy (XPS) data were obtained with an ESCALab 220i-XL electron spectrometer from VG Scientific using 300 W Al Kα radiation. Elemental compositions of the TCO sample were analyzed by inductively coupled plasma (ICP) spectroscopy using acid digestion of the TCO sample and an Optima 3000DV spectrometer. A digestion procedure with 50% HNO_3 alone or in the presence of 10% HF was performed to achieve the complete solubilization. Here, the oxygen content was calculated from the difference between sample weight and the sum of the P and Sn contributions in the sample.

2.3. Electrochemical measurements

Galvanostatic measurements were carried out using two-electrode coin cells with lithium metal as the counter electrode. The working electrodes were fabricated by uniformly compressing the mixture of 80 wt% active materials, 10 wt% acetylene black (AB) and 10 wt% polytetrafluoroethylene (PTFE) onto a copper foil at 2×10^6 Pa. The electrode sheet was cut into circles, typically 150 μm thick. The pellets of the same mass were dried in vacuum at 100 °C for at least 8 h and then assembled as coin cells in an Ar-filled Labconco glovebox. The electrolyte solution was 1 M $LiPF_6$ dissolved in a mixture of ethylene carbonate (EC), dimethyl carbonate (DMC), and diethyl carbonate (DEC) with the volume ratio of EC:DMC:DEC = 1:1:1. Charge–discharge tests were conducted at 20 °C using a Roofer Battery Tester (Shenzhen, China) operating in galvanostatic mode.

3. Results and discussion

The morphology of the product obtained was investigated by FESEM. Fig. 1a shows the FESEM image of a typical sample

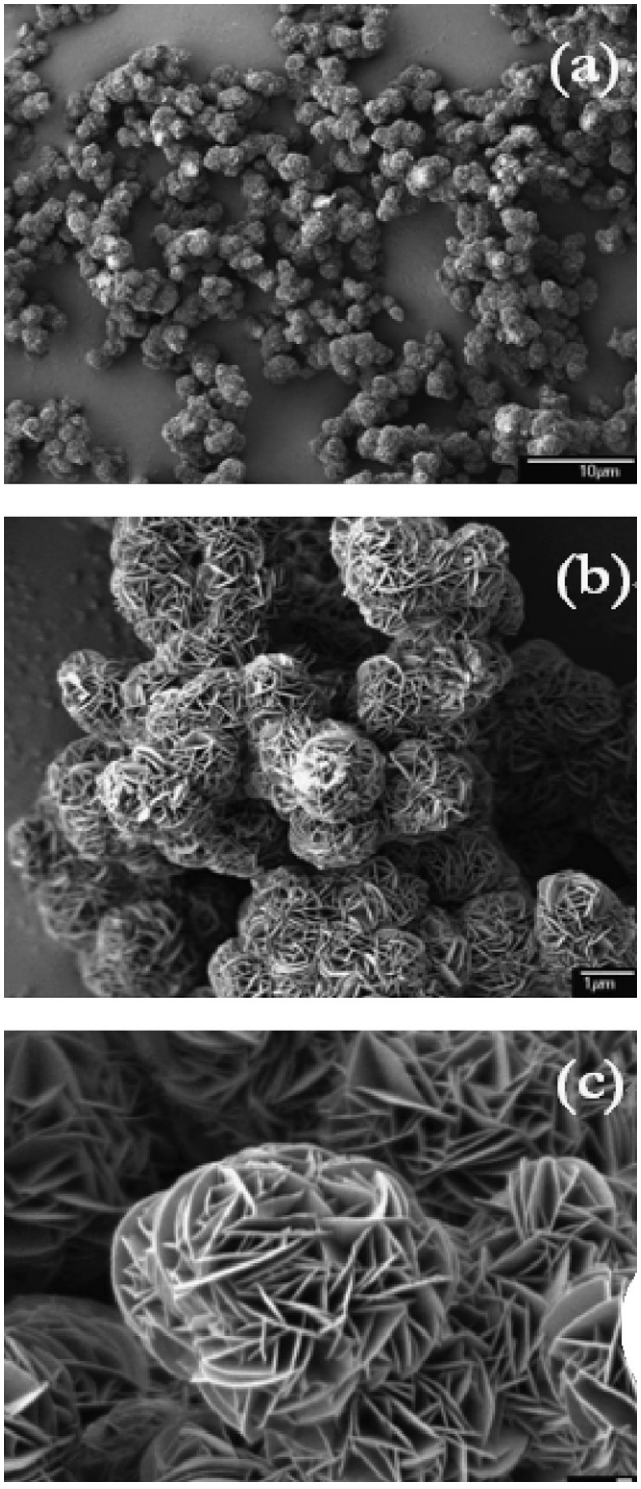

Fig. 1. FESEM images of the TCO hierarchical microspheres.

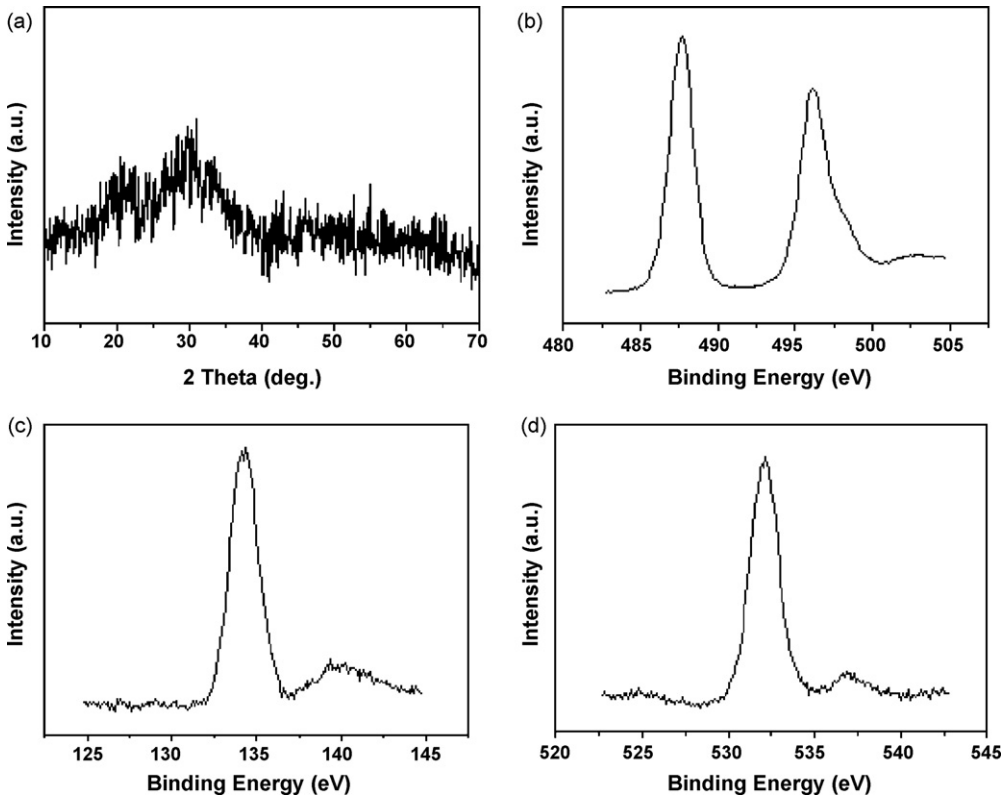

Fig. 2. (a) XRD pattern and (b–d) XPS spectra of the TCO hierarchical microspheres: (b) Sn 3d region, (c) P 2p region, and (d) O 1s region.

composed of many uniform, spherelike architectures with diameters ranging from 1.5 to 2 μm. The detailed morphologies of the spherelike architectures are shown in Fig. 1b and c, which clearly reveal that the entire structure of the architecture is built from several dozen nanoplates with smooth surfaces. As exhibited in Fig. 1c, these nanoplates are *ca.* 20 nm thick and 500 nm wide, and connected to each other to assemble into porous hierarchical microspheres. The corresponding powder XRD pattern provides structural information for the obtained product, as shown in Fig. 2a. A broad band of weak diffraction between 20° and 30° was observed, without concomitance of any diffraction line assigned to crystalline forms. This distribution is characteristic of amorphous TCO glasses, essentially similar to the previous result observed for $Sn_{1.0}B_{0.56}P_{0.40}Al_{0.42}O_{3.6}$ (average grain size of 5–10 μm) [9,15]. Our XRD intensity is generally weak and no characteristic peaks can be identified. These materials are therefore largely amorphous with low degrees of long-range order. Some examples pertaining to the finding are the tin oxides in glassy matrix ($SnB_xP_yO_z$) [9,15]. It can be observed (not shown) that the intensity of the peak slightly increased when as-obtained sample was calcined at over 400 °C temperatures under air flow. However, annealing over 400 °C of as-obtained sample would result in loss of the hierarchically microspherical morphology. Thus, in this work, 300 °C was chosen as calcination temperature in order to remove water and retain the original morphology of the hierarchical microspheres. Important information about the element composition and chemical valence of the product obtained can be provided by XPS, as shown in Fig. 2b–d. The binding energies obtained in the XPS analysis were corrected for specimen charging by referencing the C 1s to 284.6 eV. In Fig. 2b, there are two strong peaks at *ca.* 487.7 and 496.1 eV binding energies, which can be attributed to Sn $3d_{5/2}$ and Sn $3d_{3/2}$, respectively, being in agreement with the literature values for Sn (IV) in the bulk [30]. Besides, the P 2p and O 1s binding energies in Fig. 2c and d are usually centered at *ca.* 134.3 and 532.2 eV, respectively [31]. Consequently, on the basis of the quantification of Sn 3d, P 2p and O 1s peaks, our sample can be reasonably formulated as $Sn_{1.0}P_{1.17}O_{4.72}$, which is consistent with the result analyzed by ICP measurements (shown in Table 1). Structurally, Sn (IV) is supposed to form the electrochemically active center for lithium alloying and de-alloying, and the other group makes up an electrochemically inactive random network of –(P–O)– bonding that homogeneously and anisotropically delocalizes the Sn (IV) active center [15].

In order to understand the formation process of such TCO hierarchical microspheres, we carried out time-dependent experiments during which samples were collected at different time intervals. Fig. 3a–d shows the FESEM images of the samples taken from the reaction mixture at different periods of time (1, 3, 6, and 9 h at 150 °C, other conditions are the same as those described in Section 2). Such a process is consistent with previous reports of a so-called two-stage growth process, which involves a fast nucleation of amorphous primary particles followed by a relatively slow aggregation of primary particles [23,26–28]. As shown in Fig. 3a, at the early stage, the sample was composed of *ca.* 50 nm nanoparticles, which became the nuclei and quickly grew into primary nanoplates approximately 100 nm in size. In the following secondary growth stage (Fig. 3b and c), the *in situ* formed nanoplate building units gradually grew and spontaneously aggregated into

Table 1
Elemental compositions of the TCO hierarchical microspheres analyzed by XPS and ICP spectroscopy, respectively

	Sn	P	O
XPS	1.0	1.17	4.72
ICP	1.0	1.15	4.65

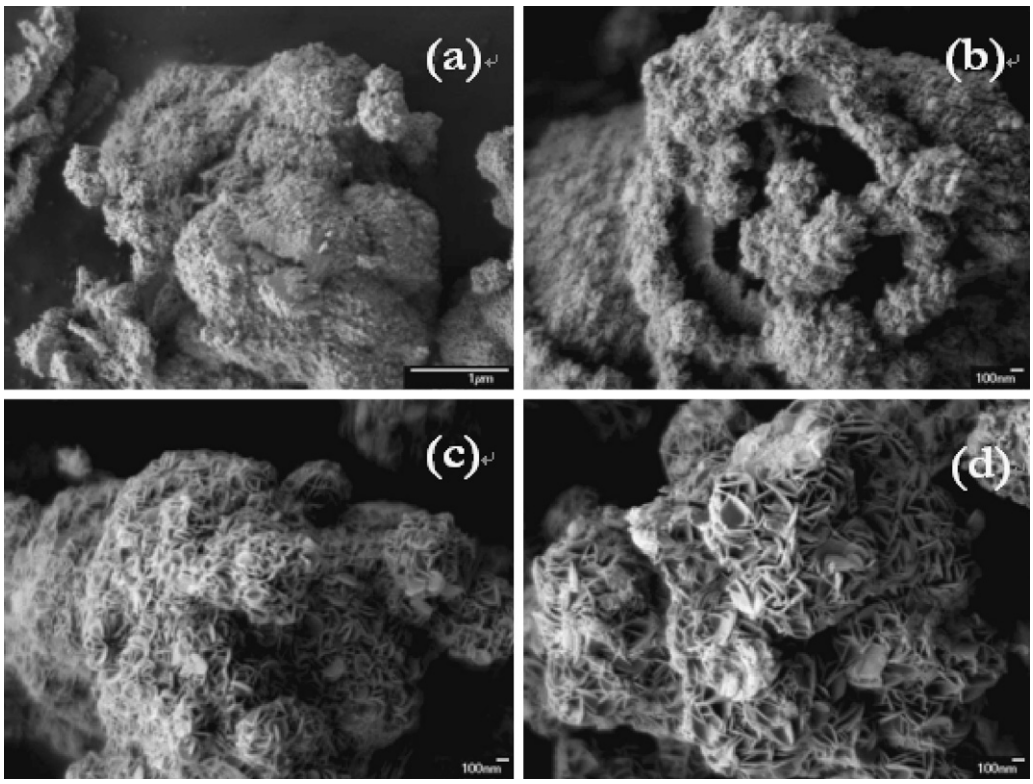

Fig. 3. FESEM images of the morphological evolution process of the TCO precursors collected at different intervals: (a) 1 h, (b) 3 h, (c) 6 h, and (d) 9 h.

ca. 500–800 nm spherelike architectures. As the reaction proceeded (Fig. 3d), these spherelike architectures continued to expand by combining with the remaining primary nanoplates, eventually forming more than 1 μm porous hierarchical microspheres with a yield of *ca.* 100%. Several factors, including electrostatic and dipolar fields associated with the aggregation, van der Waals forces, hydrophobic interactions and hydrogen bonds, may have various effects on the self-assembly processes [28]. Based on different driving mechanisms, large-scale self-assembly of low-dimensional building blocks into complex three-dimensional ordered architectures is still a challenge for material scientists.

Shown in Fig. 4a are the potential versus capacity profiles for the TCO hierarchical microspheres, cycled at a 1*C* rate (with *C* being defined as the full use of the capacity in 1 h) in the 0.005–1.5 V potential window. All reported potential values are given versus Li/Li^+ and the rate is calculated by supposing the whole active material being reduced during the first discharge. As has already been established in the previous works [4,9], the reduction of SnP_xO_y glasses by lithium consists, during the first discharge, of two separated and distinct processes that become highly intermixed upon cycling. The two-phase reaction, involving a reduction of SnP_xO_y and lithium ion to metallic tin and lithium phosphate and an alloying of the tin with lithium, can be described as follows:

$$SnP_xO_y + zLi^+ + ze^- \rightarrow Sn + Li_zP_xO_y \quad (1)$$

$$nLi^+ + ne^- + Sn \rightarrow Li_nSn \quad (0 < n < 4.4) \quad (2)$$

It can be considered that the participation of lithium-ion coordination in reversible charge–discharge reactions takes place at the bonding orbital of Sn–O, accompanied by partial electronic reduction of both Sn (IV) and Li^+, but not forming a state of metallic lithium (safe lithium-storage mechanism) [2,3,7]. The formation of the lithium phosphate and metallic tin is an irreversible reaction mainly responsible for the irreversible capacity, and the reversible alloying and de-alloying processes offer reversible storage capacity in this system. The anisotropic random network of the glass structure accounts for why there is a wide potential distribution in lithium uptake and release as exhibited by the gentle slope in the charge/discharge curves [15]. In the first discharge/charge process, the discharge capacity was about 933 mAh g^{-1} and the charge capacity was about 463 mAh g^{-1}, resulting in an initial capacity loss of about 50%. Fig. 4b shows the discharge capacities versus the number of cycles at a 1*C* rate. The cycling behavior shows a progressive "activation", which highlights a slight increase in capacity with increasing cycle numbers. The initial specific capacity was about 470 mAh g^{-1}, and was gradually increased to a maximum value of about 590 mAh g^{-1} after 6 cycles, which corresponds to nearly twice the level of existing state-of-the-art carbon materials [1]. The reversible capacity was maintained at about 514 mAh g^{-1} after 20 cycles, and the discharging capacity retention was more than 87%. This capacity retention is far superior to that of previously reported amorphous or crystalline TCO [2–9]. The analysis of the first charge and discharge potential–capacity curves shows the different steps. Compared to the case of pure SnO_2 [2,3,7], the smooth curves without the characteristic steps of the TCO are indicative of equilibration between the various phases of LiSn alloys formed during Li intercalation and deintercalation. As the current density used was relatively low, the non-observance of stepwise formation is probably not due to kinetic effects, but rather a confirmation of the amorphous nature of the TCO with a pervasive matrix. The TCO shows remarkably good capacity retention with the cell still retaining 87% of its initial oxidation capacity after 20 cycles. This is certainly much better than most of the performances previously reported for any bulk tin oxide based materials, where significant loss of reversible capacity occurs within the first 10–20 cycles [2–9]. Courtney and Dahn [3] presented results that show that the rate of tin aggregation and capacity fade decreases with increasing number of 'spectator atoms' (P) per tin atom, for a range of amorphous

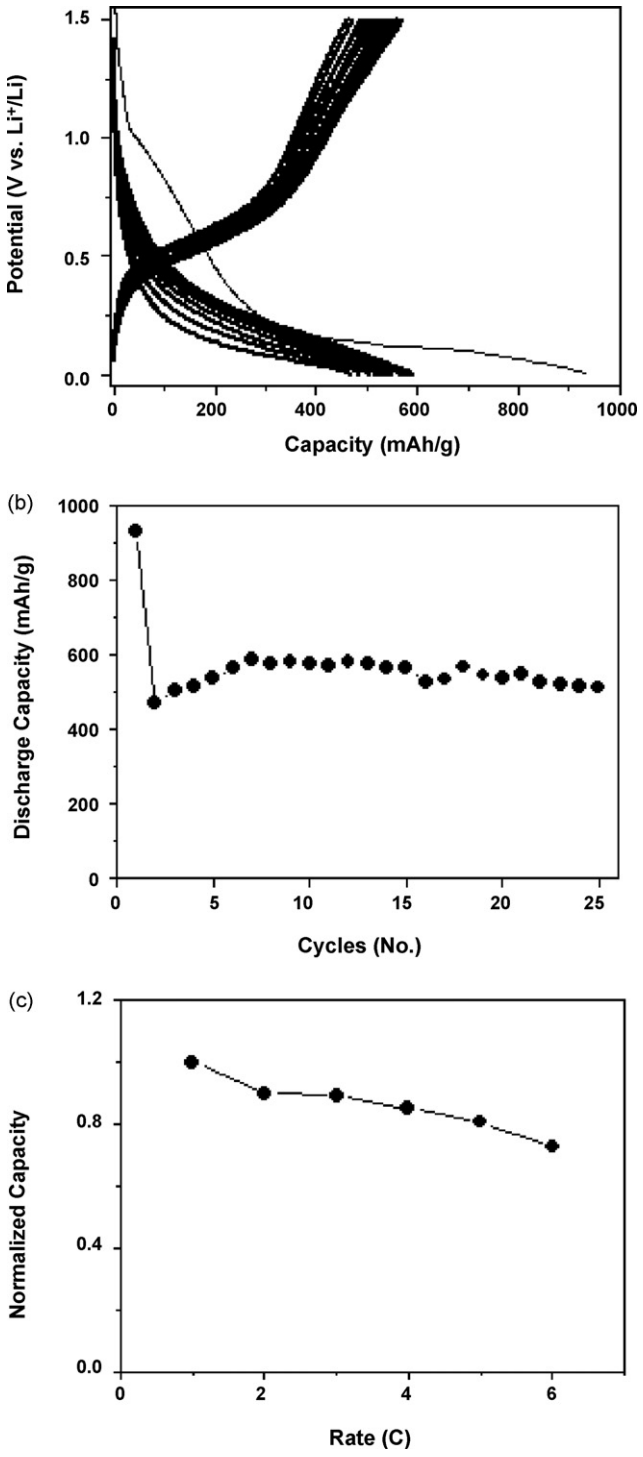

Fig. 4. Electrochemical performance of the TCO hierarchical microspheres galvanostatically cycled between 0.005 and 1.5 V vs. Li^+/Li. (a) Voltage–capacity profiles at a rate of 1*C*. (b) The corresponding plots of discharge capacity retention. (c) The normalized capacity is plotted versus rate ranging from 1*C* to 6*C*.

$Sn_xP_yO_z$ compositions. This means that there is a trade-off between good cyclability and large specific capacity. Among the TCO tested here, though the P/Sn ratio is higher than 1, this P-rich composition has little influence on the potential–capacity curves. Another performance regarding the TCO hierarchical microspheres as an electrode material is to determine the rate capability. For that, a rate capability test was planned for the electrode after its 20th discharge. Fig. 4c shows the variation of the capacity as a function of the applied rate expressed in terms of *C* over a range of 0.005–1.5 V. Strikingly, the electrode can sustain high rates and it turns out that more than 70% of the reversible capacity could be delivered even at a 6*C* rate, which has not been described previously to our knowledge. The diffusion of lithium ions is very complex because the nature of the electrolyte phase, the solid–liquid interface, the tortuosity, and the size of the electrode material has to be considered [29]. Herein we only consider the overall process by assuming that the diffusion coefficient is independent of these factors, which means that the diffusion length, *L*, can be estimated as $(Dt)^{1/2}$, where *D* and *t* are the diffusion coefficient and time, respectively. We introduced a lithium-ion pathway through the porosity obtained via nanoplate assemblies and an electronic pathway through the three-dimensional, glass-phase network by assembling nanoplates into the electrode material to give a porous microarchitecture that is able to undergo a rapid charge/discharge process, which differs from the traditional concept of lithium ion insertion/extraction into bulk crystalline materials.

The significance of these results is a demonstration that outstanding rate and cycling capability from electrochemical alloying is possible by using the unique three-dimensional porous microarchitecture with subtle nanosized features. Such hierarchical microspheres, with an interconnected network of nanoplate building blocks, facilitate the liquid electrolyte to penetrate every part of the microsphere, which expose more accessible surface sites for lithium ions to enter the microsphere and decrease the possibility of local destruction of structure due to large lithium ion flux, especially at high charge/discharge rates. Moreover, the self-assembly of the primary nanoplates throughout the microspheres also allows more facile lithium diffusion, while the internal nanoplates shorten lithium diffusion distances, which are critical features in expediting the rate capability of the microspheres by avoiding ion depletion regions or concentration gradients that can degrade cell performance. On the other hand, the porosity obtained via nanoplate assemblies within the microspheres not only help accommodate the mechanical stress resulting from the large volume change during alloying and de-alloying cycles to maintain the structure integrity, but also prevent agglomeration or growth of the tin grains, offering microstructural stability.

4. Conclusions

In summary, to benefit from the large capacity gain advantages offered by lithium-induced electrochemical alloying and to overcome poor kinetics, a novel concept to tackle such issues by using porous hierarchical microspheres with an interconnected network of nanoplate building blocks, has been introduced and demonstrated with $Sn_{1.0}P_{1.17}O_{4.72}$ glass as an example. Such desired three-dimensional microarchitectures with exciting nanosize effects can be exploited to fabricate next generation of lithium-ion batteries where outstanding rate capability and sustained reversible capacity are achieved. Such a philosophy paves the way for further advances in the efficient use of electrode materials operating through electrochemical alloying.

Acknowledgments

This work was financially supported by NSFC (No. 20628303) and 863 Project (2006AA05Z123).

References

[1] A.S. Arico, P. Bruce, B. Scrosati, J.M. Tarascon, W.V. Schalkwijk, Nature Mater. 4 (2005) 366.

[2] J.O. Besenhard, J. Yang, M. Winter, J. Power Sources 90 (2000) 70.
[3] I.A. Courtney, J.R. Dahn, J. Electrochem. Soc. 144 (1997) 2943.
[4] M. Behm, J.T.S. Irvine, Electrochim. Acta 47 (2002) 1727.
[5] K.D. Kepler, J.T. Vaughey, M.M. Thackeray, Electrochem. Solid-State Lett. 2 (1999) 307.
[6] S. Panero, G. Savo, B. Scrosati, Electrochem. Solid-State Lett. 2 (1999) 365.
[7] R. Retoux, T. Brousse, D.M. Schleich, J. Electrochem. Soc. 146 (1999) 2472.
[8] Y.W. Xiao, J.Y. Lee, A.S. Yu, Z.L. Liu, J. Electrochem. Soc. 146 (1999) 3623.
[9] J.Y. Lee, Y.W. Xiao, Z.L. Liu, Solid State Ionics 133 (2000) 25.
[10] D. Aurbach, A. Nimberger, B. Markovsky, E. Levi, E. Sominski, A. Gedanken, Chem. Mater. 14 (2002) 4155.
[11] Y.L. Zhang, Y. Liu, M.L. Liu, Chem. Mater. 18 (2006) 4643.
[12] E. Kim, D. Son, T.G. Kim, J. Cho, B. Park, K.S. Ryu, S.H. Chang, Angew. Chem. Int. Ed. 43 (2004) 5987.
[13] M. Noh, Y. Kim, M.G. Kim, H. Lee, H. Kim, Y. Kwon, Y. Lee, J. Cho, Chem. Mater. 17 (2005) 3320.
[14] E. Kim, Y. Kim, M.G. Kim, J. Cho, Electrochem. Solid-State Lett. 9 (2006) A156.
[15] Y. Idota, T. Kubota, A. Matsufuji, Y. Maekawa, T. Miyasaka, Science 276 (1997) 1395.
[16] O. Mao, R.L. Turner, I.A. Courtney, B.D. Fredericksen, M.I. Buckett, L.J. Krause, J.R. Dahn, Electrochem. Solid-State Lett. 2 (1999) 3.
[17] I.S. Kim, P.N. Kumta, G.E. Blomgren, Electrochem. Solid-State Lett. 268 (2005) 147.
[18] G.F. Ortiz, R. Alcántara, J.L. Tirado, Electrochem. Solid-State Lett. 10 (2007) A286.
[19] L. Kőrösi, S. Papp, V. Meynen, P. Cool, E.F. Vansant, I. Dékány, Colloids Surf. A 268 (2005) 147.
[20] J.M. Tarascon, C. Delacourt, A.S. Prakash, M. Morcrette, M.S. Hegde, C. Wurm, C. Masquelier, Dalton Trans. (2004) 2988.
[21] J.M. Tarascon, S. Grugeon, M. Morcrette, S. Laruelle, P. Rozier, P. Poizot, C. R. Chim. 8 (2005) 9.
[22] E.M. Sorensen, S.J. Barry, H.K. Jung, J.R. Rondinelli, J.T. Vaughey, K.R. Poeppelmeier, Chem. Mater. 18 (2006) 482.
[23] C. Burda, X.B. Chen, R. Narayanan, M.A. El-Sayed, Chem. Rev. 105 (2005) 1025.
[24] J. Du, Y. Chen, Angew. Chem. Int. Ed. 43 (2004) 5084.
[25] B. Liu, H.C. Zeng, J. Am. Chem. Soc. 126 (2004) 8124.
[26] A.M. Cao, J.S. Hu, H.P. Liang, L.J. Wan, Angew. Chem. Int. Ed. 44 (2005) 4391.
[27] C.Z. Wu, Y. Xie, L.Y. Lei, S.Q. Hu, C.Z. OuYang, Adv. Mater. 18 (2006) 1727.
[28] L.S. Zhong, J.S. Hu, H.P. Liang, A.M. Cao, W.G. Song, L.J. Wan, Adv. Mater. 18 (2006) 2426.
[29] H.S. Zhou, D.L. Li, M. Hibino, I. Honma, Angew. Chem. Int. Ed. 44 (2005) 797.
[30] N. Sharma, J. Plevert, G.V. Subba Rao, B.V.R. Chowdari, T.J. White, Chem. Mater. 17 (2005) 4700.
[31] P.S. Attidekou, P.A. Connor, P. Wormald, D.P. Tunstall, S.M. Francis, J.T.S. Irvine, Solid State Ionics 175 (2004) 185.